JOURNAL OF AIRCRAFT
Vol. 49, No. 5, September–October 2012

Wing–Body Circulation Control by Means of a Fuselage Trailing Edge

R. J. Huyssen*
North-West University (Pretoria Campus), Lynnwood Ridge 0040, South Africa
G. R. Spedding†
University of Southern California, Los Angeles, California 90089
and
E. H. Mathews‡ and L. Liebenberg‡
North-West University (Pretoria Campus), Lynnwood Ridge 0040, South Africa

DOI: 10.2514/1.C031543

Ideal flight sheds the least amount of kinetic energy into a wake while imparting momentum sufficient to balance the vehicle weight. This combination defines a unique downwash distribution for the wake, which an aircraft designer should provide for. A central fuselage, as required for the typical flight objective, presents an obstacle to this intent. A wing interrupted by a prominent fuselage is expected to shed inboard trailing vortices with central upwash harmful to the span efficiency of the aircraft. It is proposed here that a trailing edge on the fuselage can be used to control the circulation in the central region of the aircraft so that the central downwash deficiency can be avoided. Such a Kutta edge can further be applied as part of a high-lift system to increase central downwash by increasing the loading on the wing root and lift over the fuselage itself. Time-averaged flowfields behind a wing–body combination with and without a Kutta edge have been measured in wind-tunnel experiments. The results show that an edged aft-body does influence central circulation, as predicted. Flight with ideal wakes may be more readily attained than hitherto realized.

Nomenclature

AR	=	aspect ratio
b	=	wing span, m
b_b	=	spanwise extent of body, m
C_D	=	coefficient of drag
C_L	=	coefficient of lift
c	=	wing chord, m
d	=	fuselage diameter, m
l	=	fuselage length, m
n	=	number of observations for time averaging
q	=	rms of fluctuating velocity magnitude, m/s
Re	=	Reynolds number
U	=	mean freestream velocity, m/s
u	=	streamwise velocity component (disturbance velocity, with U removed), m/s
$\bar{u}$	=	time average of velocity component, m/s
v	=	spanwise velocity component, m/s
w	=	vertical velocity component, m/s
$\langle w \rangle$	=	space averaged velocity component, m/s
α	=	geometric wing angle of attack, deg
δ	=	downward Kutta edge deflection angle, deg
Γ	=	circulation, m^2/s
ν	=	kinematic viscosity, m^2/s
ω_x	=	streamwise component of vorticity

Received 12 June 2011; revision received 28 April 2012; accepted for publication 1 May 2012.

*Center for Research and Continued Engineering Development, Private Bag X30; Aeronautical Engineer, Diomedes Innovations (Pty) Limited; info@diomedes.co.za.

†Department of Aerospace and Mechanical Engineering; geoff@usc.edu. Member AIAA.

‡Contract Professors, Center for Research and Continued Engineering Development, Private Bag X30, and Consultants to TEMM International (Pty) Limited; LLiebenberg@rems2.com and ehmathews@rems2.com.

I. Introduction

THE wing with minimum induced drag has an elliptical circulation distribution $\Gamma(y)$ over the span so that the spanwise downwash $w(y)$ it induces is constant [1,2]. The flux of vertical momentum related to lift is determined by w, and the kinetic energy of the accelerated air is proportional to w^2. Therefore, the maximum momentum for minimum energy is transferred when $w(y)$ is constant, and it is simple to show that any deviation from this pattern must lead to a reduction in the lift-to-induced-drag ratio. The ideal aerodynamic shape for span efficiency of a lifting surface may therefore approximate an elliptical flying wing, with no other interfering parts (Fig. 1a). Practical flying devices must do more than occupy aerodynamic optima, and so compromises for stability and control and for carrying a payload lead to shapes in which the influence of the wing on the surrounding airflow is considerably altered by the presence of tail wings, flaps, engines, and a fuselage.

The most common arrangement for commercial transport is often termed the tube-and-wing configuration. The fuselage, shaped essentially like a long, streamlined tube, disrupts the wing. The fuselage itself is not usually designed to produce much lift, and the adverse effects of having the fuselage interfere with the wing must be tolerated as part of the design compromise. In this case, as shown in Fig. 1b, the fuselage is necessarily associated with local loss of lift ([3], pp. 11–18) and increased drag ([4], pp. 8–16). Figure 1b, analyzed in terms of either departure from constant $w(y)$ or the presence of additional streamwise vorticity, represents a more energetically wasteful solution than Fig. 1a. It would be better if the fuselage were not there.

Although the optimum aerodynamic shape for an aircraft could be that of a flying wing, the wing volume is generally insufficient to accommodate payloads of typical density and grain size ([5,6], pp. 13–16). It is possible to inflate the wing beyond aerodynamic necessity as in the various blended-wing–body (BWB) designs (e.g., [7]). However, as this approach is unsuitable for many flight objectives, this paper will retain the idea of a dedicated volume for payload, as in the typical tube-and-wing configuration. Normally, this fuselage has a flightwise length that is determined, in part, by stability and balance requirements, so that additional tail wings, both vertical and horizontal, will be mounted on the end of a relatively

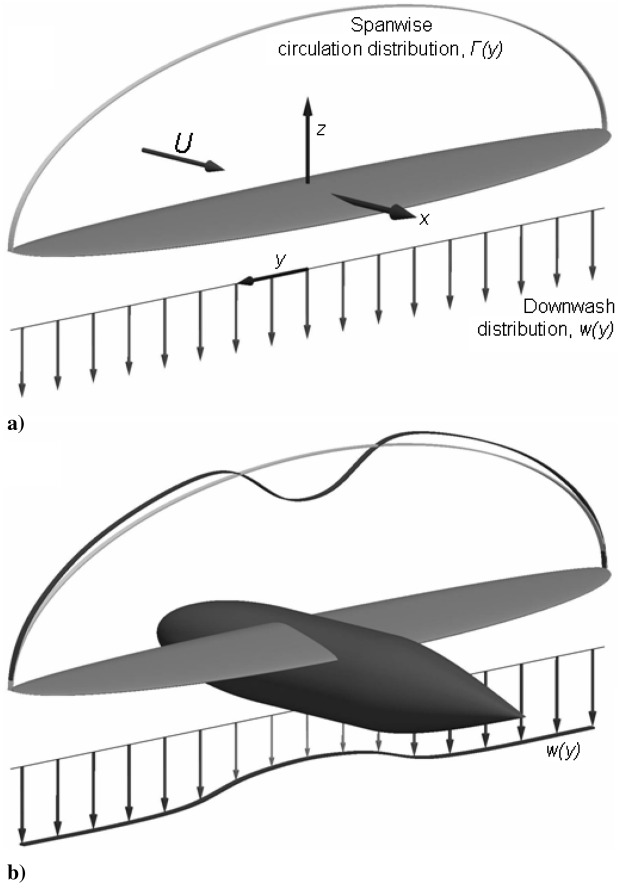

Fig. 1 Schematic representation of a) an ideal- and b) a compromised spanwise distribution of circulation $\Gamma(y)$ and downwash $w(y)$, on the basis of equal wing lift.

long tail boom or fuselage extension. The consequences of relaxing this requirement will be investigated, assuming that stability and control can be provided without separate tail wings. (A rich history of tailless aircraft ([6], Chap. 12) various BWB designs and related research on this project show this to be possible [8].)

If the fuselage is not required to accommodate tail wings far behind the aircraft center of gravity, then it is likely to be shorter and larger in diameter while retaining the elliptical cross-section of the current dominant arrangement. McCormick ([9], Chap. 4, p. 165) summarizes data indicating a broad minimum in total volume-normalized drag coefficient for fineness ratios l/d between three and six. Therefore, provided that structural implications of pressurization are considered, a much broader design space of lower l/d shapes can be exploited. The shorter, wider body also allows new strategies for proximate circulation control on the body itself.

The following section will investigate the possible modification or tailoring of the body wake, to evaluate whether the optimal uniform distribution of $w(y)$ in Fig. 1a can be restored from its suboptimal state of Fig. 1b.

II. Shaping the Circulation Distribution

The wing–body aerodynamics can be described interchangeably either in terms of the spanwise circulation distribution $\Gamma(y)$ or the spanwise downwash distribution $w(y)$. The unique value of the local circulation on a lifting wing is determined by the Kutta condition at the trailing edge. If a prominent body interrupts the wing trailing edge, then the Kutta condition will not, in general, be maintained over the body itself, and the local circulation will change. (Defining a clear Kutta condition or an expected equivalent for a three-dimensional flow over a tapered pointed body is not obvious.) Any spanwise gradient in $\Gamma(y)$, $\partial\Gamma/\partial y$ must be accompanied by shedding of streamwise vorticity, and sharp changes in the gradients in $\Gamma(y)$ will be visible as variations in $w(y)$ in the near wake. Such variations in $w(y)$ can be used as diagnostics of the quality of $\Gamma(y)$.

Wing–body interference may alter the circulation at the wing root, and body circulation may exist such that the total lift of the wing–body combination may increase, as found in wind-tunnel tests of [10–14], reported by Hoerner ([4], pp. 8–17). However, such lift increment comes, necessarily, with an extra cost of lift-induced drag, due to the suboptimal spanwise variation in $\Gamma(y)$ of the combination, unless a deliberate effort is made to shape the wake. Together with additional parasite drag, the total drag of the wing–body combination is higher than that of the wing alone. Hoerner ([4], pp. 8–18) reports an increment in induced drag expressed as $\Delta C_{Db} = 0.035(\Delta C_{Lb})^2$ where the ratio of spanwise extent of the body b_b to total span b (b_b/b) ranges up to 0.2. (Here C_{Db} and C_{Lb} are based on the body-occupied planform area, cb_b.)

As proponents of BWB configurations have long noted, considerable induced drag reductions can be expected if the body geometry is designed to support, maintain, and control a nonzero circulation profile [7,15]. According to these same arguments, it also ought to be possible to provide control surfaces along the aft edge of a semistreamlined body. The pressure drag may remain significant, but streamlines do not depart very far from the outline, so that the rear stagnation point can be fixed. Furthermore, in principle, the rear stagnation line location could be made to match the condition on the wing root. In this case, to a near-wake observer, the downwash profile across the span (including the body) has little or no trace of the body. Fixing the rear stagnation line in this manner is equivalent to forcing some nonzero circulation on the body itself, which now becomes a lifting body and dynamically part of the wing. From the perspective of shedding streamwise vorticity, the vorticity shed by the body edge would have an opposite sign and approximately equal magnitude to vorticity shed from the wing root. The result will be an even $w(y)$ profile with little spanwise variation.

Described here are the initial experiments to test the hypothesis that a suitable body-circulation-control device can be deployed to modify the circulation on the body and effectively erase its inviscid signature in the wake. Although there exist a variety of concepts by which circulation control can be implemented [16,17], the detail of implementation is beyond the scope of this initial work. The device chosen for this study is referred to as a fuselage Kutta edge (KE), as it is expected to enforce the Kutta condition on the flow over the entire fuselage. A wing–body–KE combination can be shown to approach the ideal wing-alone wake quality.

III. Equipment and Methods

A. Wind Tunnel and Model

A low turbulence ($q/U \leq 0.03\%$ [18,19], where q is the root mean square of the velocity fluctuations) closed-loop wind tunnel with an octagonal test section of 1.36 m inscribed diameter was used at sea-level conditions. A rectangular, symmetric, untwisted wing with a NACA 0012 airfoil with a 76 mm chord c and 500 mm span b ($AR = 6.6$) was supported vertically at the wingtips between the top and the bottom walls of the test section. The bottom support sting was attached to a rotary table by which the geometric angle of attack α could be set to within ± 0.05 deg. The sting protruded from the lower wingtip with a diameter of 4.5 mm for the first 50 mm before tapering to the sting diameter of 8 mm. Because of this flow obstruction on the lower wingtip, the observation volume captured the top half of the model (above the plane of symmetry) where the tip support was far less obstructive. The top wingtip was supported by a pair of solid steel wires of 0.3 mm diameter splitting at 30 deg off the vertical to the sides of the top window of the test section. Model oscillations and vibrations were avoided by applying a suitable tensile prestress to these supports. The top support did not restrict the rotational degree of freedom needed to alter the model angle of attack.

A fuselage could be added to this wing in a variety of arrangements. Tests described here had the wing–body in a shoulder wing arrangement. The wing was rigged at 6 deg with fillets typical of

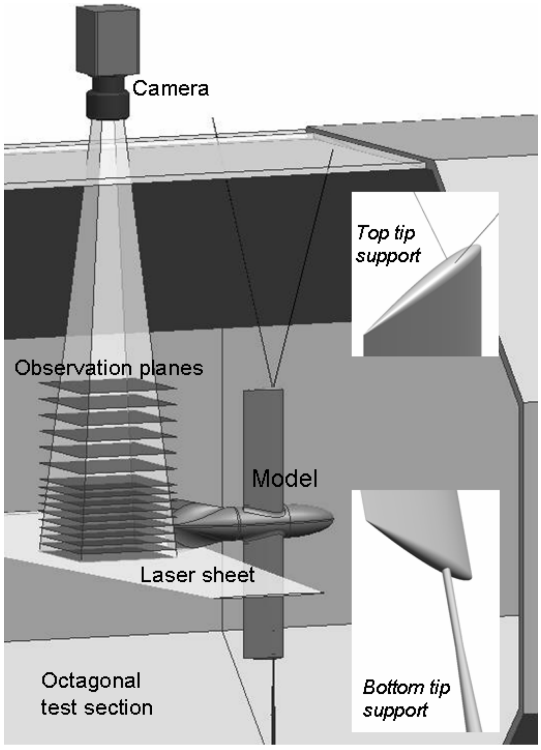

Fig. 2 The wind-tunnel model is vertically supported between a vertical sting and a pair of 0.3 mm steel wires. A vertically synchronized camera and laser sheet scan the observation volume in a smoke-seeded closed-loop wind tunnel from just below the model plane of symmetry to just beyond the upper wingtip.

the tube-and-wing arrangement. The fuselage, essentially a circular body with a diameter $d = 60$ mm, blanked off about 12% of the wing span ($d/b = b_b/b = 0.12$). The fineness ratio was $l/d = 5.5$, with a nose cone of length $1.7d$, a cylindrical section of $1.7d$, and a tail cone of $2.1d$. The tail cone could be fitted with a flat plate of any shape to provide a fuselage trailing edge. In these tests the KE had a span of 102 mm ($0.2b$) and formed a leading edge on the side of the tail cone with a sweep angle of 78 deg. This flat plate was blended with the tail cone, as visible in several figures. The aft body could be deflected to offer adjustability of the KE angle. A schematic of the experimental setup appears in Fig. 2, with details of the model shown in Fig. 3.

For optical reasons, the model was coated in nonreflective black. Matte black spray paint was applied to the wing, and the fuselage was taped over with a rough black adhesive tape. A trip wire of 0.6 mm diameter was placed on the wing upper surface at about $0.22c$ and around the fuselage at the wing trailing edge ahead of the tail cone, the pressure recovery region of the fuselage. These measures were taken in an attempt to force flow transition in the low-Reynolds-number boundary layer to improve the conditions for the flow to remain attached or to reattach.

B. Flow Visualization Setup

A dual-head Nd:YAG laser emitting a pair of coaxial laser beams was used to illuminate oil-based smoke in a horizontal sheet about 4 mm thick behind the vertically mounted model. A dual-frame Kodak ES4.0 CCD camera captured a pair of square images at a resolution of 1024×1024 pixels, exposed for less than 5 ns each with typically 180 μs between the two laser shots. With an 85 mm 1:10 Nikon lens positioned 1.3 m from the observation plane, the square observation frame captured 192×192 mm, and the freestream displacement ($U = 10$ m/s) had a mean pixel displace-

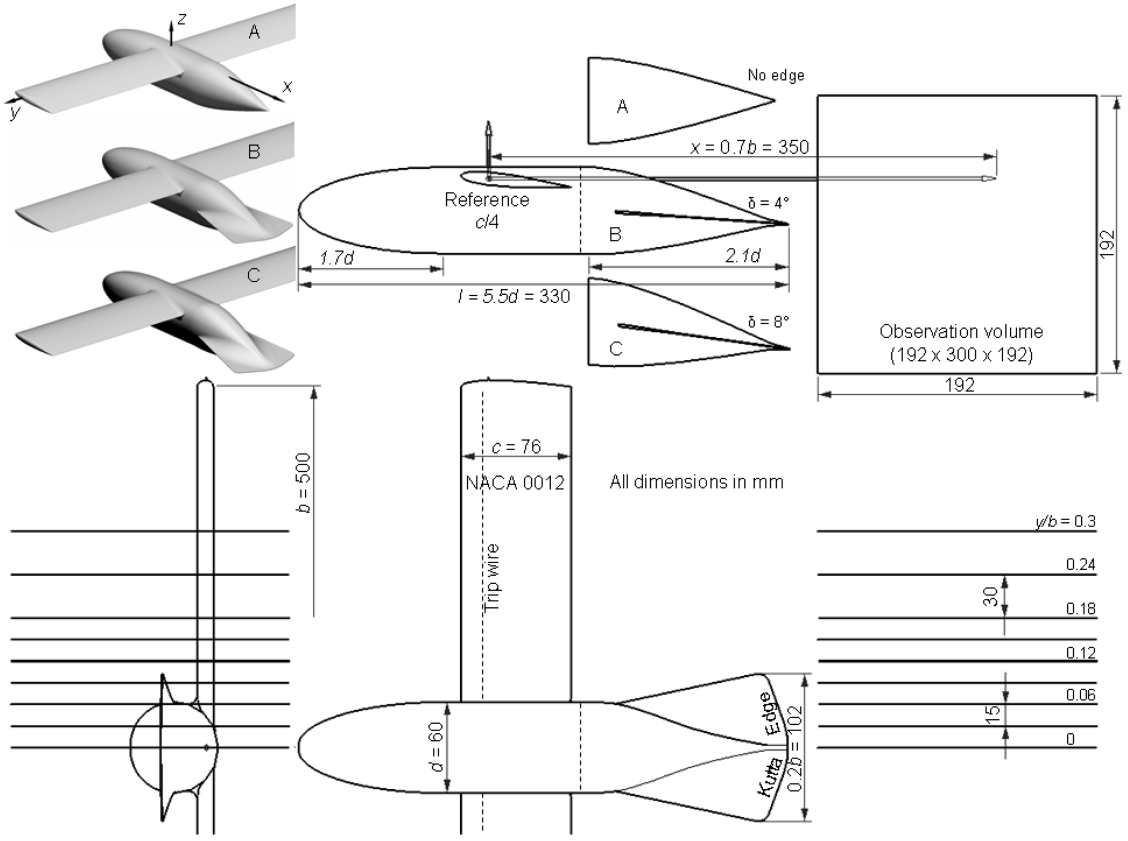

Fig. 3 After testing only the rectangular wing, a body was added rigged at 6 deg in the shoulder-wing arrangement. After testing the combination with the pointed fuselage without a trailing edge (A), a KE was added. Then the tail cone was deflected down by 4 deg (B) and later to $\delta = 8$ deg (C). The observation planes used in this report are shown here to scale in their relative positions. Streamwise averages were derived around $x = 0.7b$ behind the reference point.

ment of approximately 9.6 pixels. Fifty frame pairs were taken at a rate of 4.8 Hz at each test station. Synchronized vertical traversing of the camera and the laser sheet provided the means for the spanwise scan of the observation volume.

C. Test Matrix

Initial tests were conducted with the wing alone. This provided the baseline for comparisons with wing–body geometries illustrated in Fig. 3. The fuselage without a KE was then added to the wing (model A in Fig. 3). For the reference tests described here, the fuselage axis was parallel to the freestream flow, thus giving a wing angle of attack $\alpha = 6$ deg.

For the next series of tests the KE was added to the fuselage tail cone. Three different KE incidence angles were tested, $\delta = 0, 4$, and 8 deg down from the freestream axis. The latter two are models B and C in Fig. 3, respectively. The $\delta = 0$ deg case provided confirmation that the KE did in fact alter the flowfield, but in an undesirable way. The $\delta = 4$ deg case had the KE at an angle slightly less than that of the wing (rigged at 6 deg), whereas $\delta = 8$ deg held it at slightly more. It was anticipated that the two cases would demonstrate a useful trend in wake modification.

Every test commenced with the wing angle of attack $\alpha = 0$ deg (thus with the body axis at -6 deg), with the first observation plane three stations below the model plane of symmetry. After acquiring 50 frame pairs, the spanwise position of the observation frame was changed until reaching the last station beyond the wingtip. The angle of attack was then increased by 2 deg and the spanwise scan was repeated in reverse. This was repeated until $\alpha = 8$ deg. In this way all five cases (wing-only, no edge, and $\delta = 0$, 4, and 8 deg) were tested under the same test conditions.

D. Processing

A customized variant of the correlation imaging velocimetry (CIV) algorithms of [20] was used to estimate the displacement field from each frame pair. A most-likely cross-correlation function is estimated by fitting an average of two spline-interpolated autocorrelation functions calculated from the same correlation subwindows in the two images of each pair. The range of possible displacements of a correlation window is completely separated from the window dimensions itself, and arbitrary shifts can be added or subtracted to take into account mean background flows. The bandwidth of the correlation displacements is thus optimized about the disturbance velocity field and not for the mean. Estimated displacements were moved to a location halfway along the displacement vector, and were then reinterpolated onto a regular grid of 65×66 grid points, using the two-dimensional spline-interpolation algorithms described by Spedding and Rignot [21].

During postprocessing, the true mean freestream velocity U, as derived from the observed flowfield, was subtracted from each $\{U + u, w\}(x, z)$ field to yield the disturbance flowfield $\{u, w\}(x, z)$ as induced by the model. Images aligned with the vertical aircraft axis z and parallel to U give the disturbance velocity components u and w in x and z. Each of the 50 $\{u, w\}$ field estimates was inspected in its 4290 grid points, and obvious flaws were removed before calculating the time average over the 10.4 s period to yield the time averaged disturbance flowfields $\{\bar{u}, \bar{w}\}(x, z)$. The multiple planes in the spanwise direction y of $\{\bar{u}, \bar{w}\}(x, z)$ formed the basis for subsequent analysis.

The data from these observation frames were then assembled into three-dimensional data sets for import into the flow visualization tool ParaView. By visualizing the entire flowfield in the observation volume, a qualitative but global understanding could be obtained as to how the various model changes affected the wake. This provided the focus and context for more selected quantitative comparisons. Of the five test cases the $\delta = 0$ deg case is not included in the description of the data in this report. Of the five tested angles of attack only the 6 deg reference case is used here as representative of an aircraft in a steady cruise condition with the body aligned with the flow. Of the 15 spanwise stations, the outer stations, which appeared to be beyond the influence of the body and the KE, have been excluded from this report.

IV. Limits and Accuracy

A. Experimental Limitations

The purpose of this investigation was to distil the equivalent of the simplified schematic presentation of Fig. 1 from actual experimental data and then to test the influence on such downwash distributions by the addition and manipulation of the fuselage trailing edge. Although it was to be determined whether the cause of wake deterioration of a wing–body combination could in principle be removed by means of fuselage trailing edge manipulations, no attempts were made to precisely remove this cause or even to quantify the changes in drag. Useful drag measurements are difficult to obtain, and here only small changes to induced drag are expected, which, at this scale, are overwhelmed by complex viscous issues. Similarly, it was reasoned that little could be gained to verify predictions from measurement of lift. Force measurements were taken for preparatory purposes alone and therefore are not included in this discussion.

1. *Observation Volume*

The schematic representation of Fig. 1b qualitatively shows an effect in the inviscid field as induced by the complex flow interactions with an air vehicle. Although it is sufficient to observe the induced effect in the inviscid disturbance field to discover departure from or return to the ideal wake of Fig. 1a, it is useful to understand the cause of such changes. The affected field is huge and the measurable disturbance varies considerably with relative location to the model. In comparison to the inviscid disturbance field, the viscid disturbance is limited to a very small portion of the affected field trailing from the solid boundaries of the model. Because the disturbance of shed vorticity approximately coincides with this viscous wake, flow observations had to include this region. However, the key observations come only from the inviscid disturbance field above and below the viscous wake (see Fig. 4).

A spanwise stack of longitudinal frames formed the observation volume, as illustrated in Fig. 2. In this orientation, the entire optic array could be mounted rigidly and free from any contact with the wind tunnel. None of the equipment was exposed to the airflow, and the flowfield was completely unobstructed. However, in this arrangement the spanwise component v was unobservable and only the velocity components $\{u, w\}$ in streamwise (x, z) planes could be estimated. These components are in the direction of drag and lift, respectively. The streamwise vorticity, $\omega_x = \partial w/\partial y - \partial v/\partial z$, was therefore also unknown. The local magnitude of $\partial w/\partial y$ could not be reliably estimated from the coarse discretization in y (also the $\partial v/\partial z$ component was unavailable), and so the focus was exclusively on the larger scale spanwise variation $w(y)$ where the time-averaged distribution was measured reliably and repeatably through the multiple spanwise slices.

Comparative investigations could be performed from the estimated disturbance vectors in some 64,000 grid points within the total observation volume. Although this yielded high-density information, the total volume is small in comparison to the volume of flow affected by the model. It was therefore not feasible to derive the global magnitudes of the influence under investigation. However, comparative tests were on an equal basis.

2. *Low Reynolds Number*

With the freestream velocity $U = 10$ m/s over the chord $c = 76$ mm and with ν the kinematic viscosity, the $Re = Uc/\nu$ was on the order of 45,000. Model and tunnel size, model support considerations and smoke seeding limitations restricted data collection to this low Re. Because the basic arguments are made in the usual aeronautical context in which Re is assumed to be large, certain special precautions were taken to ensure that the test objectives could be achieved.

The global disturbance field reflects the influence induced by the pressure field around the model, whereas only a small fraction of the

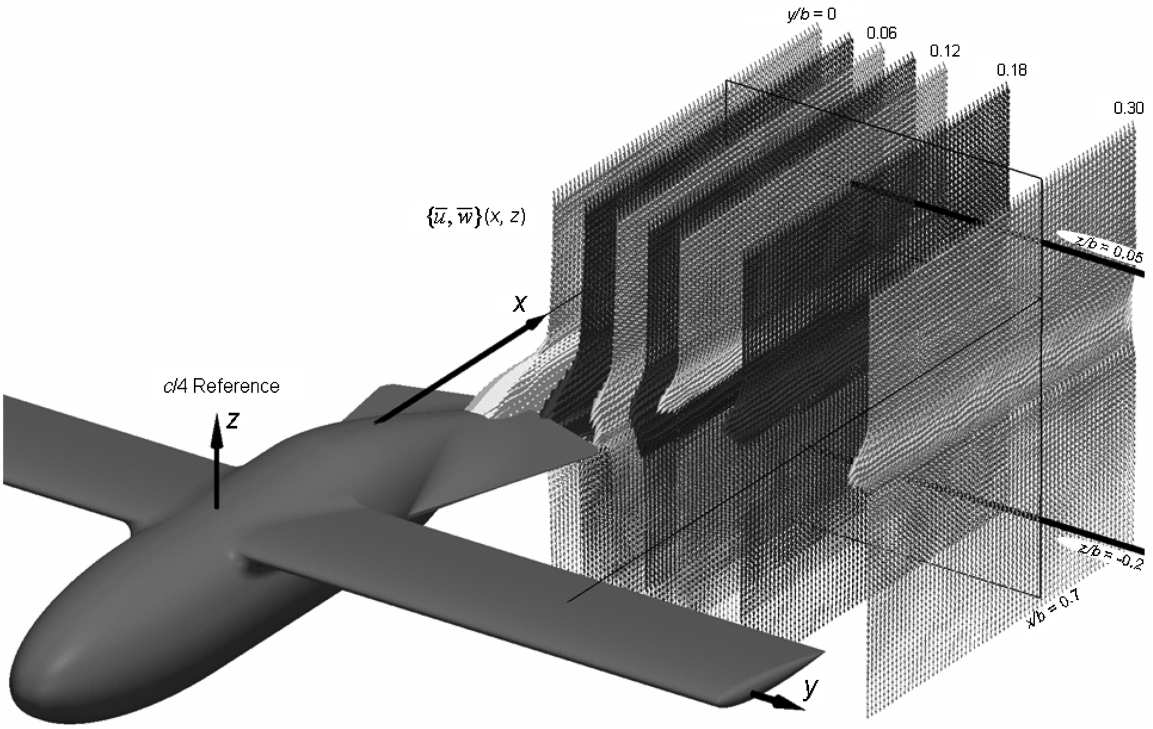

Fig. 4 Flow vectors were estimated in 65 × 66 (4290) grid points in each of 15 (x, z) observation planes (of which seven are shown here). Removal of the freestream velocity from time-averaged estimates yielded the disturbance fields $\{\bar{u}, \bar{w}\}(x, z)$ in which the viscous wake is here clearly visible just below the reference z plane. Spanwise downwash distributions of Figs. 6 and 8 were derived from streamwise averages take around $x = 0.7b$ in the vertical locations shown above and below the viscous wake.

wake shows the traces of the viscous interactions with the model. Therefore, the proposed phenomena should be observable in the global disturbance field if the pressure field is representative of that of a typical full-scale aircraft in subsonic flight. Furthermore, as long as the Kutta condition holds on all relevant trailing edges (implying that the rear stagnation remains on the relevant trailing edge), even in the presence of separation, the circulation should be representative of a field in which separation is absent. Therefore, a range of wing angles of attack was chosen ($\alpha = 0$ to 8 deg), at which reasonable wing circulation prevailed. During preparatory experiments lift measurements were used to establish the lift curves for the wing-only case. Combined with CIV observations on the wing upper surface, the absence of problematic flow separation on the wing could be confirmed.

The same could not be done for the fuselage because the circular cross-section and awkward optical reflections obscured the boundary-layer regions from CIV images. It therefore had to be assumed that flow separation was likely to prevail in the pressure recovery region of the fuselage, just behind the wing trailing edge, given the low *Re*. However, if the fuselage is observed to affect the circulation in the central region of the wing–body arrangement, it would be hard to explain how the absence of separation could leave wing circulation intact. Furthermore, the downwash defect of wing–body arrangements at high *Re* has been observed by others (e.g., Jacobs and Ward [10]). After adding the KE and deflecting the aft body down, flow separation could become even more problematic, but again, the absence of separation would be in favor of the phenomena to be observed. If the phenomenon is observable in the presence of separation at low *Re*, then it should be reasonable to assume that it will be observable under more favorable conditions in the absence of separation at any higher *Re*.

3. Averaging

Flow at such a low *Re* is unsteady in the viscous wake (as shown by Spedding and McArthur [22]), but quantitative measurements can be derived from suitable time and space averages [23]. Extensive preparatory work was done to select appropriate setup parameters and to choose a proper observation volume size and location. This work was primarily conducted on the wing-only case and also involved force measurements. Here each spanwise observation was made in four streamwise stations starting on the wing itself. For higher data density, a smaller observation frame was used, given the smaller obstruction in the flow. Angle-of-attack sweeps of larger range and smaller increments were used to observe separation patterns on the wing and to observe their streamwise trails. Sensitivity studies were conducted to find an appropriate number of observations n as a basis for time averaging. Results presented here used $n = 50$ frame pairs. This showed convergence of the downwash statistics well within this data length for various separation patterns. Even in the unsteady wake of separation, convergence of disturbance magnitudes was reached within $n = 30$, and in outer wake regions convergence had already been reached with $n = 10$. Here $\bar{w}$ is the time average of the downwash w in each grid point.

Time-averaged data were further smoothed by space averaging over a streamwise portion, Δx. Initial investigations showed that the measurement of vertical downwash profiles was insensitive to the streamwise location, provided that a consistent location was used for the comparisons. Therefore the last of the four streamwise stations of the wing-only case was used for all further observations. Cases that included the body required a larger observation frame clear of the body and the KE. Streamwise data averaging was performed in the overlapping portion of the different observation frames, and so it was done around $x = 0.7b$ (downstream of the quarter chord, $c/4$, reference of the wing) over a streamwise portion of $\Delta x = 0.2b$, as illustrated in Fig. 5. Then $\langle \bar{w} \rangle$ is the streamwise space average over Δx of the time average of w taken from 50 estimates over a period of 10.4 s at a rate of 4.8 Hz.

B. Experimental Accuracy and Reliability

In a well-designed experiment, CIV-based estimates of the in-plane velocity components can be resolved to within 5% of their true value, and uncertainties in estimation of spatial gradients can be within 10% [20]. No explicit use of gradient quantities is made here, and all the data are obtained exclusively from time averages. Thus,

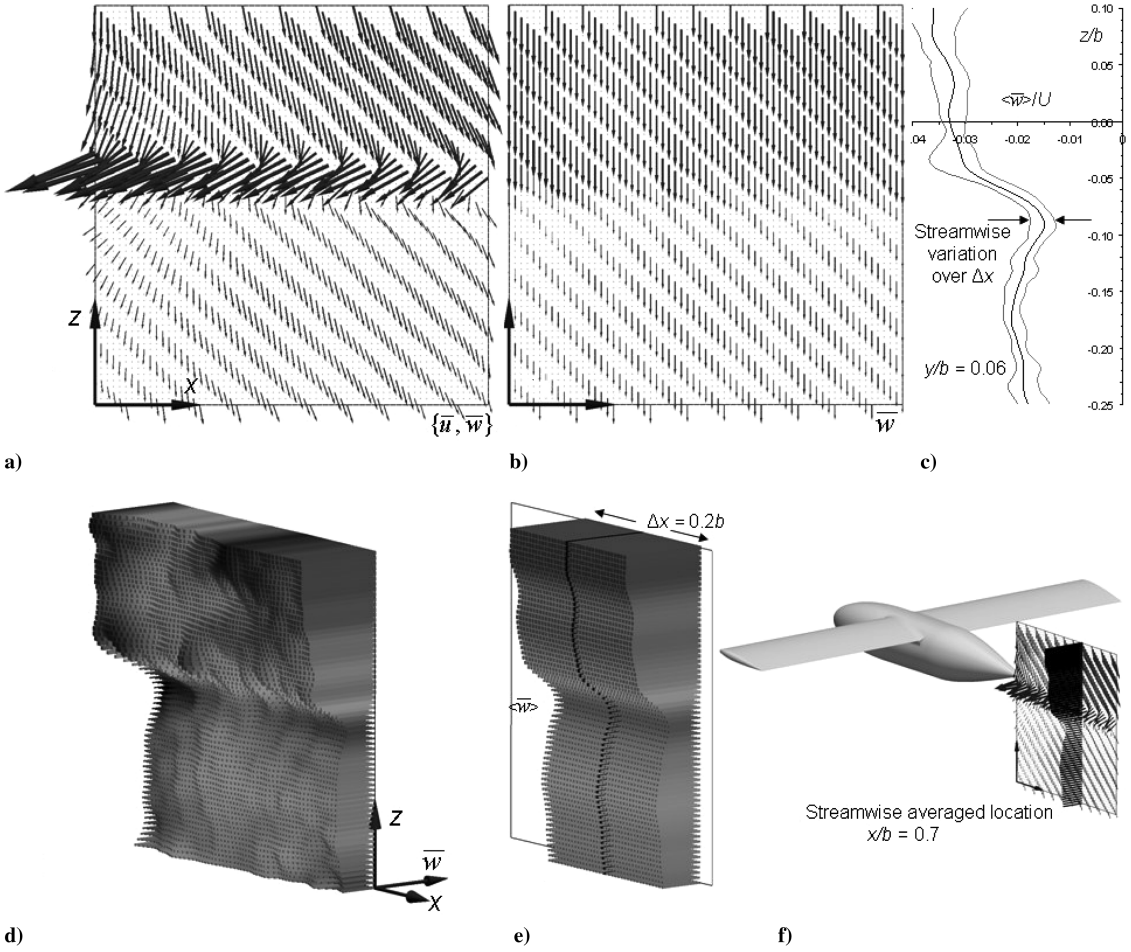

Fig. 5 From the time-averaged disturbance velocity field $\{\bar{u}, \bar{w}\}(x, z)$ in a) the downwash, $\bar{w}(x, z)$ is isolated, shown as a vector field in b) and again as a surface in d) (formed by perpendicular bars of downwash magnitude). Residual fluctuations in $\bar{w}$ are removed in e) by streamwise averaging over the illustrated portion of data (Δx). The resulting mean vertical downwash profile $\langle \bar{w} \rangle(z)$ is quantified in c) between the bands of maximum and minimum values within Δx. The relative position to the model is shown in f).

the level of confidence with which to evaluate the data may be indirectly assessed, as any single observation made at every single grid point over a period of time is acquired in complete independence of any other. Therefore, the relative similarity of such observations, both in terms of neighbors as well as post- and predecessors, offers a measure of confidence in the reliability of the observation.

The absolute accuracy depends on numerous aspects of the experimental setup and procedures. Proper control over lighting uniformity, particle seeding density, image brightness, and freestream uniformity are all critical components that are necessary for the claimed uncertainties [24]. In addition, there are certain systematic deviations from ideal geometry, involving optical distortions and small uncertainties in light-plane orientation, that degrade the absolute accuracy. However, in comparative measures of time-averaged velocities, the time-averaged data can be reliable to within 1% [20].

In comparative measures of time-averaged velocities, repeated measurements (from different days) of mean flow and peak defect velocities were within $\pm 1\%$ of each other. The same measurement setup has been shown to yield flat plate drag coefficients to within 5% of their theoretical value from interrogation of mean defect profiles, and mean flow quantities are checked against those derived from pitot static tube measurements each day.

V. Results

A. Data Reduction Sequence

Figure 5 shows, by means of one sample observation, the data reduction sequence that provides the basis for the comparative wake survey. Figure 5a shows a typical vector map $\{\bar{u}, \bar{w}\}$ of a disturbance field in the (x, z) plane, as derived by removing the mean freestream velocity component U and time averaging over 50 CIV estimates in each of the 4290 grid points (of which only every sixth vector is shown in Figs. 5a and 5b). Figure 5b shows the isolated downwash component $\bar{w}$ after removal of the $\bar{u}$ component, which previously made the viscous wake of the wing and body clearly visible.

In Fig. 5d the downwash field $\bar{w}(x, z)$ is again displayed, now as a surface formed by perpendicular bars of downwash strength in each grid point. Small-amplitude residual fluctuations are noticeable close to the body, but those farther downstream are negligible, and in Fig. 5e, these have been removed by averaging over a cropped portion of the data in only the streamwise direction x as described previously.

The resulting streamwise-averaged vertical downwash profile $\langle \bar{w} \rangle(z)$ is repeated in nondimensional form, $\langle \bar{w} \rangle / U$ against z/b, in Fig. 5c. Here the inner line shows the streamwise average $\langle \bar{w} \rangle$ and the bounding lines show the limits of streamwise variation of $\bar{w}/U(z)$ over the averaged portion of the data. The vertical reference in Fig. 5c coincides with the $c/4$ reference of the wing. The relative position of the sample observation frame is shown in Fig. 5f. Its spanwise location is at $y/b = 0.06$, a vertical plane tangent to the side of the round fuselage without a KE.

Such streamwise-averaged profiles of $\langle \bar{w} \rangle(z)$ will be compared for the four different configurations: wing-only, wing with body (no edge), and body with KE at $\delta = 4$ and $\delta = 8$ deg. Henceforth, only the time- and space-averaged downwash $\langle \bar{w} \rangle$ will be considered, but the overbar and the brackets will be dropped for simplicity. In Fig. 6 such average vertical downwash distributions are displayed in their respective spanwise positions for the different test cases.

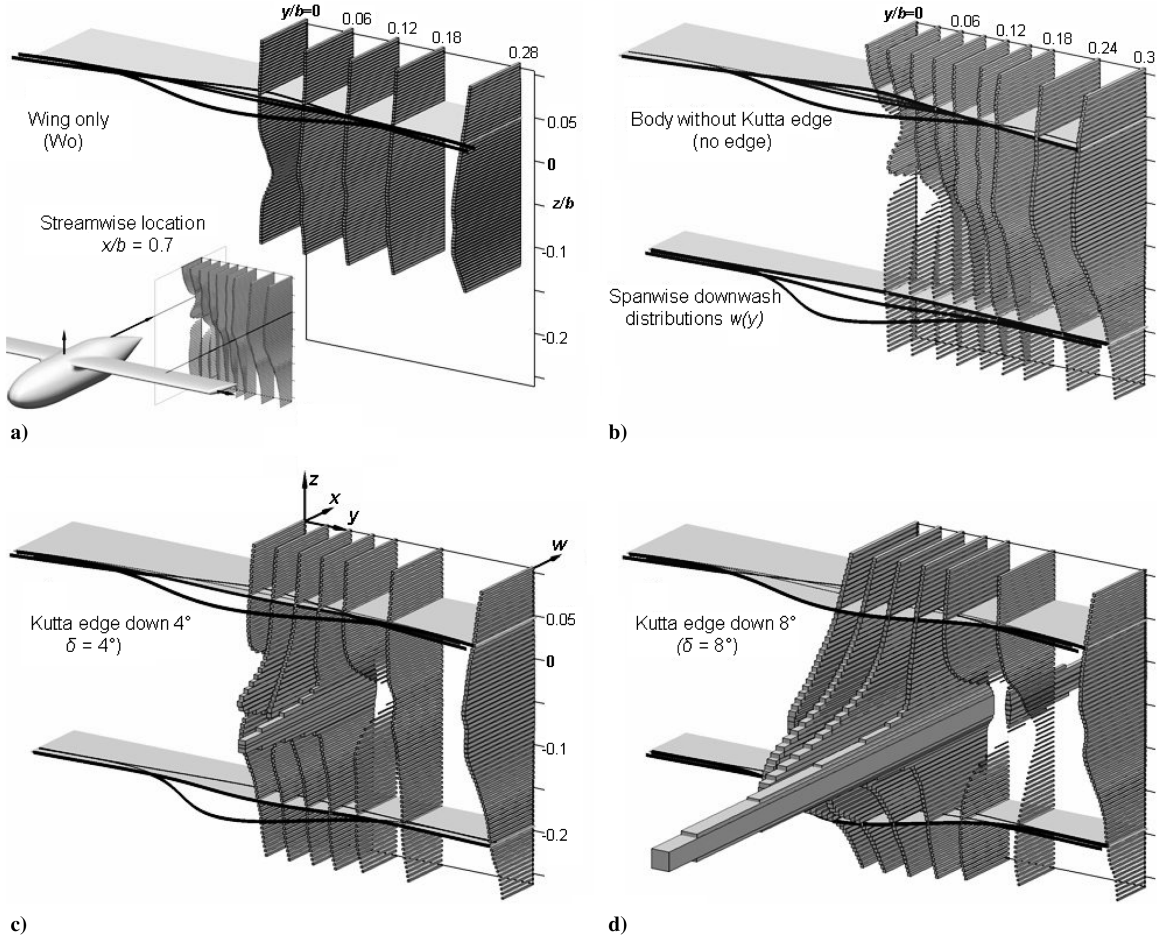

Fig. 6 Vertical downwash profiles (as derived in the previous figure) have been assembled at their spanwise locations to show the complex downwash landscapes in the (y, z) plane for the four test cases. (Note, the bars of downwash magnitude are now aligned with the x axis, with upwash being positive.) Ribbons of spanwise downwash distributions $w(y)$ are shown at two vertical locations, $z/b = 0.05$ and -0.2 (above and below the viscous wake region). These are mirrored across the plane of symmetry and all are superimposed in each landscape for comparison. These ribbons are repeated, more appropriately orientated in Fig. 8. The insert shows the downwash landscape in its relative position (comparable to Fig. 4).

B. Effect of Fuselage with Trailing Edge on Near Wake

A summary and sample of the effect of the fuselage and the KE on the wake is given in Fig. 6, which is arranged to show how representative spanwise downwash profiles alone can eventually be used to compare with the simplified prediction of Fig. 1.

The vertical downwash profiles, as described in Fig. 5, are assembled in their relative positions along the span to illustrate the downwash landscape in a (y, z) plane in $x/b = 0.7$ downstream of the $c/4$ point of the wing. Again perpendicular bars show the magnitude of downwash (with bars in the direction of x representing upwash). The downwash profiles of the wing-only at $\alpha = 6$ deg (Fig. 6a) are quite uniform along the span y and in the vertical direction z. There is no evidence of any inner trailing vortex cores (given the absence of any up- and downwash peaks that would otherwise be expected close to a vortex core).

A slight reduction in downwash due to viscous momentum transfer by the wing is visible in each vertical profile. This defect indicates the vertical location of the viscous wake, washed down slightly below the reference plane at $z/b = 0$. (The larger deficiency in the central plane is found in the disturbance trail caused by exposed fuselage mounting holes in the center of the wing.) The slight increase in downwash toward the tips is to be expected from a rectangular untwisted wing (unlike the constant spanwise downwash of the untwisted elliptical wing of Fig. 1a). Also the almost symmetrical reduction in downwash in the vertical profiles, when departing from the vertical location of the viscous wake, is in line with expectations.

When the body without the KE is added to the wing (Fig. 6b), a prominent upwash peak appears in the central plane (clearly visible in Fig. 7a) together with a downwash peak in the neighboring plane (at $y/b = 0.03$). This is consistent with the presence of a trailing vortex core somewhere between these planes. This is in line with the expectation that the Kutta condition will break down due to the discontinuity in the initial vortex sheet in the portion of the wing now occupied by the fuselage.

It appears that this central trailing vortex pair induces the downwash deficiency observable in the lower portion of the central wake as far out as $y/b = 0.12$. Although downwash above the wing is not affected by much (a slight decrease in the central region and even an increase toward the wingtips), the near vertical symmetry of the wingonly case has been lost with a downwash deficiency clearly visible in the lower portion of the distorted landscape of Fig. 6b. This distortion/variation in $w(y, z)$ will inevitably come with an induced drag penalty when compared to a wing-only case on the basis of equal lift. These observations are consistent with predictions of Fig. 1, and are quite consistent with classical data reported by Hoerner and Borst ([3], pp. 20–14) and Hoerner ([4], pp. 8–16]).

Figures 6c and 6d show the same wing-fuselage combination after the KE has been added and deflected downward by $\delta = 4$ and $\delta = 8$ deg, respectively. The spanwise downwash defect caused by the pointed body in Fig. 6b has been largely removed in Fig. 6c, and the central downwash is even increased slightly. The higher KE deflection in Fig. 6d produces a strong increase in central downwash, and now the wing–body–tail combination is increasing the total lift.

A careful tuning of deflection angle, δ, and tail shape and size is beyond the scope of this initial study, but the near-restoration of normal downwash profiles by $y/b = 0.18$ for the $\delta = 4$ deg case

shows that the flow has been returned close to the condition of the wing alone, and the inviscid body wake signature has almost been removed. The removal of the adverse influence of the body on the wake, and its commensurate reduction in the induced drag penalty, can be considered either from the point of view of evening out the $w(y)$ wake profile, or of a change in wing–body–tail $\Gamma(y)$ distribution so that trailing vortices shed by the positively loaded body–tail exactly cancel out the wing root vortices of opposite sign.

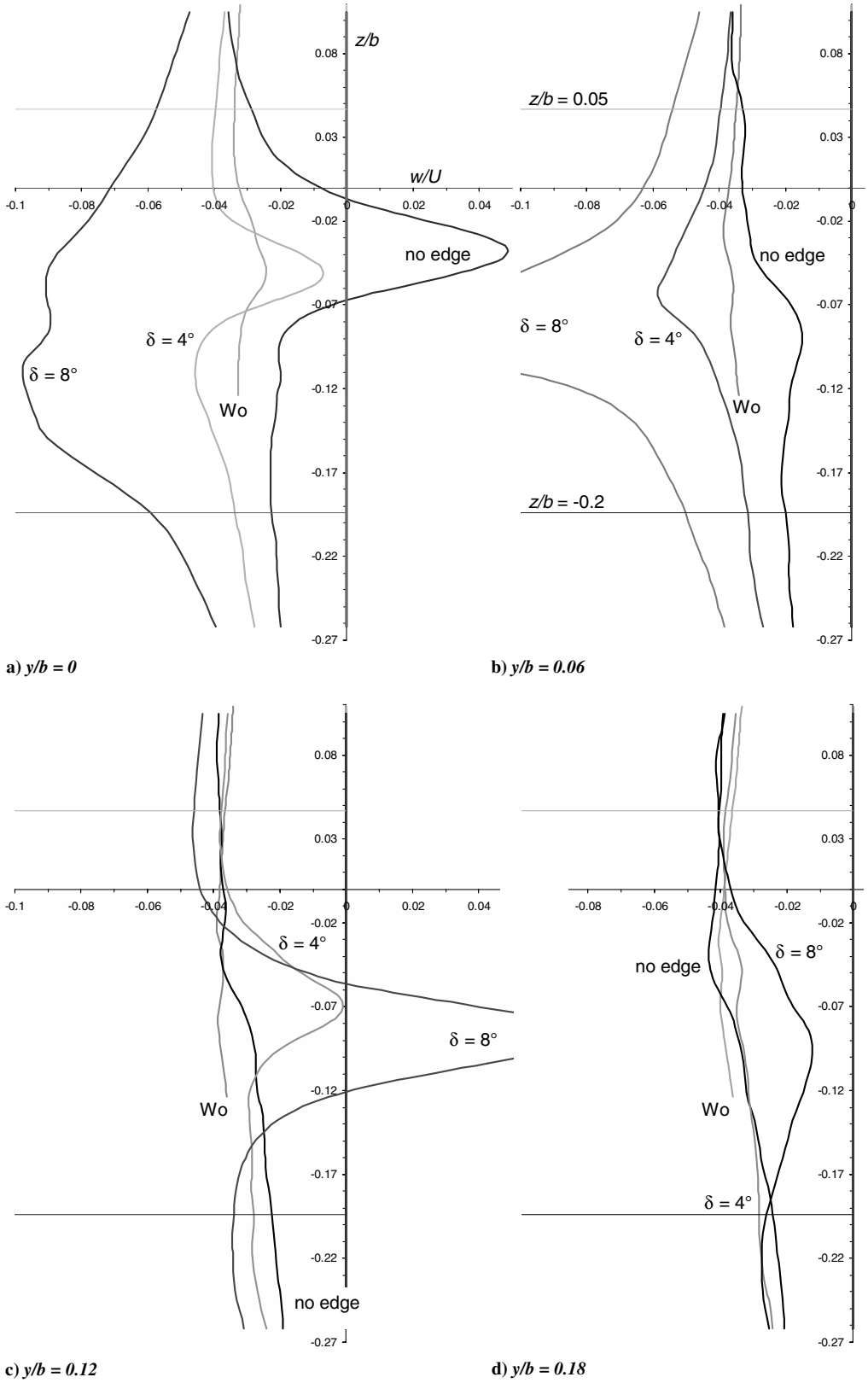

Fig. 7 Vertical downwash profiles $w(z)$ of the four cases are shown superimposed at various spanwise locations. The KE tip is located between $y/b = 0.06$ and 0.12 (visible in Figs. 3 and 8), and the peaks in the profiles of opposing direction in b) and c) for the cases with the KE are consistent with the presence of trailing vortices of different strength. The upwash peak in the plane of symmetry reveals a trailing vortex of opposite direction behind the fuselage without the edge. In the core region between the vertical limits shown, high local downwash intensities are found close to the trailing vortex cores. Therefore, the downwash distributions of the previous and the next figure have been derived outside this core region.

In either formulation, for the ideal case a downwash survey behind the aircraft will find no evidence of any inner vortex cores or of the body itself.

Each panel in Fig. 6 also repeats the progressive reconstruction of spanwise downwash distributions $w(y)$ as shown by the superimposed ribbons in two different vertical locations. The top location ($z/b = 0.05$ above the vertical reference) and the lower location ($z/b = -0.2$) have been chosen close to (but beyond) the viscous wake region. Profiles extracted any closer to the vortex cores would show strong distortions due to the intense local disturbances. From Fig. 7 it can be derived that profiles from farther beyond this region would qualitatively show the same trend. These profiles provide the experimental equivalent of the schematic predictions of Fig. 1.

For comparison, Fig. 7 superimposes the vertical downwash profiles $w(z)$ of the four cases at four different spanwise locations. At $y/b = 0$ (Fig. 7a), the strong upwash peak described previously is visible for the case of the fuselage without the KE (no edge). By contrast, the case with the KE fully down ($\delta = 8$ deg) shows very strong downwash in the central plane, whereas the case with the KE halfway down ($\delta = 4$ deg) is intermediate between the two and compares more closely with the wing-only case. When going from about halfway to the KE tip ($y/b = 0.06$, Fig. 7b) to just beyond the KE tip ($y/b = 0.12$, Fig. 7c), local downwash peaks turn to opposite peaks. It follows that these longitudinal planes lie on either side of a trailing vortex core shed from the lifting body–tail combination. The peak intensity is much smaller for the $\delta = 4$ deg case, suggesting than an even smaller deflection may yield a wake without such peaks and thus without a central trailing vortex core.

Farther out, from $y/b = 0.18$ (Fig. 7d), the downwash begins to converge and the influence of the fuselage with or without the KE has almost disappeared. It should be noted that this is well beyond the lateral extent of the fuselage ($y/b = 0.03$), even well beyond the span of the KE ($y/b = 0.1$). The two vertical locations ($z/b = 0.05$ and -0.2) from which the spanwise distribution profiles of Figs. 6 and 8 were derived are also indicated in Fig. 7.

C. Control of Wing–Body Circulation with a Kutta Edge

Figure 8 summarizes the effect of a deflected KE on the wing–body–tail wake and represents the experimental equivalent to Fig. 1. The upper downwash distributions include the wing-only case, and it can be seen that the addition of the body without the KE (no edge) reduces the central downwash, as predicted in Fig. 1b. Deflecting the KE to $\delta = 4$ deg restores the downwash profile close to the original, wing-only condition. When $\delta = 8$ deg, the tail becomes a high-lift device and the central downwash is increased significantly. If the $\delta = 4$ deg configuration is described as a return to an effective wing-only condition, then the $\delta = 8$ deg case is analogous to a high-lift device such as a trailing edge flap.

VI. Discussion

A. Implementation of a Fuselage Kutta Edge

The experiment confirmed that manipulations of the KE have a profound effect on the wake structure, and it appears possible, in principle, to find KE configurations in which any nonviscous downwash deficiency caused by a fuselage can be corrected to improve span efficiency. Success would be confirmed here by uniform spanwise downwash and/or absence of traces of inner streamwise vortex cores. The KE can also be used as part of a high-lift device. With appropriate matching to the wing circulation, any adverse wing root trailing vortices may be cancelled by an appropriately configured KE. It will be the responsibility of the designer to implement such strategies compatible with stability and balance requirements.

It would be useful to study the movement of the center of pressure in response to body edge modifications and changes in angle of attack. Insight into the influence on the aircraft neutral point by such a body edge would be equally useful.

Although significant further research will be required before the KE can be implemented as a practical method to control wake quality, these features appear to be well established and consistently implemented in the natural flight of birds, and possibly bats too.

B. Potential Consequences of Implementation

Assuming that pitch trim can be obtained by other means [8], it is conceivable to use a fuselage KE to control wake quality in order to maintain the highest possible span efficiency during all flight conditions. Additionally, as a dynamic part of a high-lift system, such a facility can significantly improve wing effectiveness. When used appropriately in conjunction with a high-lift device on the wing, a constant spanwise distribution of stronger downwash may be maintained with the help of a fuselage trailing edge. Downwash behind the fuselage implies that the fuselage contributes, as a result of a favorable pressure distribution, to the total aircraft lift. Such lift would not come from the edge feature alone but from the entire body, of which the forward stagnation line is controlled by the KE. This will permit a reduction in wing size for a given design objective. This may be significant for wide bodies (large b_b/b) of reduced fineness ratio and should easily offset any additional wetted surface required to form the trailing edge feature. Together with

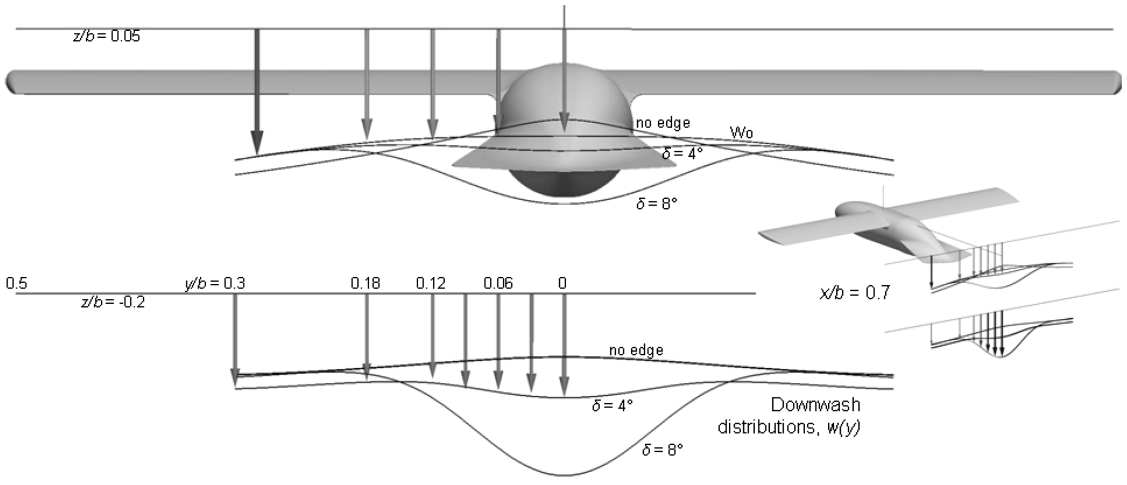

Fig. 8 The spanwise downwash distributions $w(y)$ of Fig. 6 are repeated here in their two vertical locations for the different test cases. This is the experimental equivalent of the schematic representation of Fig. 1. Note how far the influence on the downwash distribution by the body (with or without edge) extends along the span.

improved wing-bending moments, the preceding factors combine to reduce aircraft mass and wetted surface, resulting in improved aerodynamic efficiency.

If the adverse effect of the fuselage can be eliminated as proposed, the aircraft designer may employ a fuselage much wider than commonly used, and fineness ratios can be decreased toward the subsonic optimum of 3:6 (Hoerner [4], pp. 6–19, and McCormick [9], Chap. 4, p. 165). Nothing prohibits the retention of an elliptical fuselage cross-section to avoid compromising structural efficiency related to pressurization or volumetric efficiency for accommodating payload. The fuselage of smaller fineness ratio can often accommodate the same payload in a smaller total volume, depending on payload grain size. This has positive implications for both wetted surface and structural mass. The tube-and-wing configuration can be retained to benefit from its general suitability, and elaborate wing–body blending will not be required.

Finally, a fuselage fitted with such a body edge has been shown to be statically stable, as demonstrated by many applications in air and water. This reduces the responsibility of other features to provide such stability for the fuselage.

The preceding implies that the implementation of a well-designed circulation control system can make direct and indirect contributions to aircraft efficiency in several distinct ways:

1) The wing becomes more effective and it can therefore be smaller and lighter, with less wetted area.

2) The fuselage contribution to lift reduces the wing size and bending moments resulting in a smaller and lighter wing, with less wetted area.

3) The fineness ratio of the fuselage can be optimized to reduce fuselage wetted area.

4) The total fuselage volume can be reduced in favor of a lighter fuselage with less wetted area.

5) The wake quality can be improved for a better span efficiency.

6) The statically stable fuselage reduces the demand on other stabilizing features.

Taken together, the potential exists for a higher efficiency limit, allowing improvement of the mass ratio of the payload to carrier mass, the total wetted surface, and the wake quality beyond that possible using the current design approach. This is the basis for the speculation that a hypothetical ideal aircraft configuration will include a feature comparable in function and effect to the described fuselage KE.

VII. Conclusions

The experiment confirmed that the addition of a fuselage to a wing induces an adverse distortion of the wake, which, on the basis of equal lift, inevitably introduces a penalty in induced drag. Adverse inner trailing vortices have been suspected as the cause of wake deterioration. Convincing evidence of such vortices has been observed in the correlation imaging velocimetry data.

Furthermore, the experiment confirmed that the addition of a fuselage trailing edge has a profound effect on the wake, even well beyond its own spanwise extent. The wake pattern does indeed respond prominently to manipulations of the fuselage Kutta edge (KE). Such manipulations strongly affect the location and strength of inner trailing vortices and allow for their direction to be reversed. This allows the speculation that an appropriate KE arrangement can be provided by which adverse inner trailing vortices can be avoided altogether when adding a fuselage of typical shape to a wing. Thus, span efficiency does not need to be compromised by a practical fuselage.

The experiment also confirmed that total downwash can be increased significantly by means of the fuselage KE, again beyond its own spanwise extent. This allows the speculation that a KE could be a useful part of a high-lift system.

Besides the speculation that the implementation of a well-designed circulation-control device will offer several secondary benefits, it is concluded that flight with an ideal wake should be possible for wing–body aircraft configurations. The fuselage KE may be the key feature in such an achievement.

Acknowledgments

The wind-tunnel experiments were supported by an internal Research Innovation Fund at University of Southern California. We are most grateful to the University of Southern California wind-tunnel team: Shanling Yang, Vaasu Swaminathan, Travis Metzger, Aditya Vaidyanathan, Benjamin Ackerman, Austin Reed, Shiladitya Mukherjee, and Keith Holmlund, for invaluable assistance in setting up and running experiments; and to Raine Lidbetter of North-West University for assistance with both model preparations and data processing. We thank Charles Crosby for his supportive numerical work and advice on data visualization. Douglas Velleman is thanked for contributing to the manuscript.

References

[1] Munk, M. M., "The Minimum Induced Drag of Aerofoils," NACA TR-121, 1923.

[2] Jones, R. T., *Wing Theory*, Princeton Univ. Press, Princeton, NJ, 1980, Chap. 7, pp. 105–128.

[3] Hoerner, S. F., and Borst, H. V., *Fluid-Dynamic Lift: Information on Lift and Its Derivatives in Air and Water*, Hoerner Fluid Dynamics, Bakersfield, CA, 1985, Chap. 11, p. 18.

[4] Hoerner, S. F., *Fluid-Dynamic Drag: Theoretical, Experimental and Statistical Information*, Hoerner Fluid Dynamics, Bakersfield, CA, 1965, Chap. 8, p. 16.

[5] Torenbeek, E., "Aerodynamic Performance of Wing–Body Configurations and the Flying Wing," Society of Automotive Engineers Paper 911019, 1991.

[6] Nickel, K., and Wohlfahrt, M., *Tailless Aircraft in Theory and Practice*, Edward Arnold, London, 1994, Chap. 1.3, p. 19.

[7] Portsdam, M. A., Page, M. A., and Liebeck, R. H., "Blended Wing Body Analysis and Design," AIAA Paper 97-2317, June 1997.

[8] Agenbag, D. S., Theron, N. J., and Huyssen, R. J., "Pitch Handling Qualities Investigation of the Tailless Gull-Wing Configuration," *Journal of Aircraft*, Vol. 46, No. 2, 2009, pp. 683–691. doi:10.2514/1.39755

[9] McCormick, B. W., *Aerodynamics, Aeronautics and Flight Mechanics*, 2nd ed., Wiley, New York, 1995, Chap. 4, p. 165.

[10] Jacobs, E. N., and Ward, K. E., "Interference of Wing and Fuselage from Tests of 209 Combinations in the NACA Variable-Density Tunnel," NACA TR 540, 1935.

[11] Sherman, A., "Interference of Wing and Fuselage from Tests of 28 Combinations in the NACA Variable-Density Tunnel," NACA TR 575, 1937.

[12] Sherman, A., "Interference of Wing and Fuselage from Tests of 17 Combinations in the NACA Variable-Density Tunnel: Combinations with Special Junctures," NACA TN 641, 1938.

[13] Sherman, A., "Interference of Tail Surfaces and Wing and Fuselage from Tests of 17 Combinations in the NACA Variable-Density Tunnel," NACA SR 98, 1939.

[14] Sherman, A., "Interference of Wing and Fuselage from Tests of 30 Combinations with Triangular and Elliptical Fuselages in the NACA Variable-Density Tunnel," NACA TN 1272, 1947.

[15] Qin, N., Vavalle, A., and Le Moigne, A., "Spanwise Lift Distribution for Blended Wing Body aircraft," *Journal of Aircraft*, Vol. 42, No. 2, 2005, pp. 356–365. doi:10.2514/1.4229

[16] Gad-el-Hak, M., *Flow Control: Passive, Active and Reactive Flow Management*, Cambridge Univ. Press, Cambridge, 2000, Chap. 14, p. 318.

[17] Cattafesta, L. N., and Sheplak, M., "Actuators for Active Flow Control," *Annual Review of Fluid Mechanics*, Vol. 43, 2011, pp. 247–272. doi:10.1146/annurev-fluid-122109-160634

[18] Spedding, G. R., McArthur, J., Rosen, M., and Hedenstrom, A., "Deducing Aerodynamic Mechanisms from Near- and Far-Wake Measurements of Fixed and Flapping Wings at Moderate Reynolds Number," AIAA Paper 2006-33, Jan. 2006.

[19] McArthur, J., "Aerodynamics of Wings at Low Reynolds Numbers: Boundary Layer Separation and Reattachment," Ph.D. Dissertation, Univ. of Southern California, Los Angeles, 2008.

[20] Fincham, A. M., and Spedding, G. R., "Low-cost, High-Resolution DPIV for Measurement of Turbulent Fluid Flow," *Experiments in Fluids*, Vol. 23, No. 6, 1997, pp. 449–462. doi:10.1007/s003480050135

[21] Spedding, G. R., and Rignot, E. J. M., "Performance Analysis and Application of Grid Interpolation Techniques for Fluid Flows," *Experiments in Fluids*, Vol. 15, 1993, pp. 417–430.

[22] Spedding, G. R., and McArthur, J., "Span Efficiencies of Wings at Low Reynolds Numbers," *Journal of Aircraft*, Vol. 47, 2010, pp. 120–128. doi:10.2514/1.44247

[23] Spedding, G. R., and Hedenstrom, A. H., "PIV-Based Investigations of Animal Flight," *Experiments in Fluids*, Vol. 46, 2009, pp. 749–763. doi:10.1007/s00348-008-0597-y

[24] Spedding, G. R., Hedenstrom, A. H., and Johansson, L. C., "A Note on Wind-Tunnel Turbulence Measurements with DPIV," *Experiments in Fluids*, Vol. 46, 2009, pp. 527–537. doi:10.1007/s00348-008-0578-1